SCIENTIFIC REP⚙RTS

OPEN

Phase Equilibria, Crystal Structure and Hydriding/Dehydriding Mechanism of $Nd_4Mg_{80}Ni_8$ Compound

Qun Luo[1], Qin-Fen Gu[2], Jie-Yu Zhang[1], Shuang-Lin Chen[1,4], Kuo-Chih Chou[1] & Qian Li[1,3]

In order to find out the optimal composition of novel Nd-Mg-Ni alloys for hydrogen storage, the isothermal section of Nd-Mg-Ni system at 400 °C is established by examining the equilibrated alloys. A new ternary compound $Nd_4Mg_{80}Ni_8$ is discovered in the Mg-rich corner. It has the crystal structure of space group $I4_1/amd$ with lattice parameters of $a = b = 11.2743(1)$ Å and $c = 15.9170(2)$ Å, characterized by the synchrotron powder X-ray diffraction (SR-PXRD). High-resolution transmission electron microscopy (HR-TEM) is used to investigate the microstructure of $Nd_4Mg_{80}Ni_8$ and its hydrogen-induced microstructure evolution. The hydrogenation leads to $Nd_4Mg_{80}Ni_8$ decomposing into $NdH_{2.61}$-MgH_2-$Mg_2NiH_{0.3}$ nanocomposites, where the high density phase boundaries provide a great deal of hydrogen atoms diffusion channels and nucleation sites of hydrides, which greatly enhances the hydriding/dehydriding (H/D) properties. The $Nd_4Mg_{80}Ni_8$ exhibits a good cycle ability. The kinetic mechanisms of H/D reactions are studied by Real Physical Picture (RPP) model. The rate controlling steps are diffusion for hydriding reaction in the temperature range of 100~350 °C and surface penetration for dehydriding reaction at 291~347 °C. In-situ SR-PXRD results reveal the phase transformations of Mg to MgH_2 and Mg_2Ni to Mg_2NiH_4 as functions of hydrogen pressure and hydriding time.

Solid-state hydrogen storage was considered as the safest and most effective way to use the H_2 as prominent energy carrier in the future[1]. Magnesium-based alloys have been extensively investigated as potential materials for solid-state hydrogen storage due to its reasonably high hydrogen capacity (7.6wt.%) and could be interesting if it is considered as a heat storage material in heat power plants[2]. However, the relatively slow kinetics of H/D reaction makes them far from practical application. Extensive efforts have been made to improve the H/D properties of magnesium-based alloys by adopting novel preparation techniques[3,4] to reduce the particles sizes or/and adding catalytic components such as transition metals (Ni[3], Nb[5], Ti[6]) and rare earth elements (RE = La[7], Ce[8], Pr[9], Nd[10]). The addition of RE into Mg-based hydrogen storage alloys facilitates hydrogen absorption through the formation of rare earth hydrides (REH_x). The REH_x act as active nucleation sites for magnesium hydride by chemisorbing hydrogen atoms and transferring them to the Mg-metal interfaces[7,11]. Among the catalytic elements, Nd shows good catalytic effect on the H/D kinetics of Mg-Ni alloys, especially for the samples of ultrafine crystalline and small particle size[10,12–19]. Tanaka et al.[12] found that the nanocrystallized Nd-Mg-Ni alloys prepared through melting-spinning followed by crystallizing exhibited excellent hydrogen absorbing kinetics and Pressure-Composition-Temperature (PCT) characteristics in comparison with those of the corresponding as-cast alloys with coarse eutectic structures. However, the growth up of the grain size would impair

[1]State Key Laboratory of Advanced Special Steels, Shanghai University, Shanghai 200072, China. [2]Australian Synchrotron, 800 Blackburn Rd, Clayton 3168, Australia. [3]Institute of Genomic Material, Shanghai University, Shanghai 200444, China. [4]CompuTherm, LLC, Madison, WI 53719, USA. Correspondence and requests for materials should be addressed to Q.L. (email: shuliqian@shu.edu.cn)
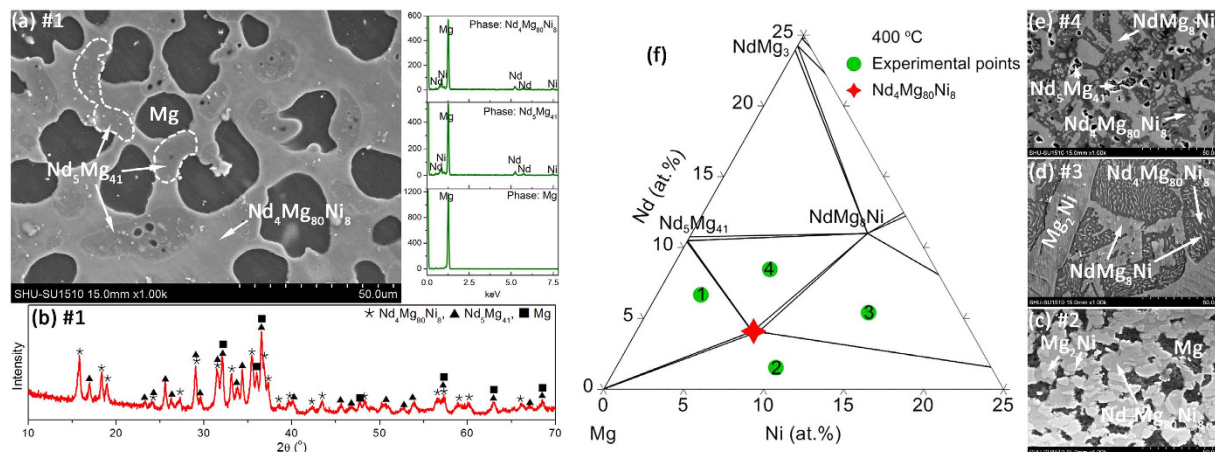
Figure 1. (**a**–**e**) The SEM images and XRD pattern of samples and (**f**) the isothermal section of Nd-Mg-Ni system in the Mg-rich corner at 400 °C.

the hydrogen storage performance. Denys *et al.*[20] found that the kinetic properties and cyclic stabilities of nanostructured Mg-based and Mg-8wt.%Mm-20wt.%Ni based hydrides degraded due to the grain growth of Mg nanocrystalline during thermal desorption above 300 °C. Therefore, it is important to keep the grain sizes of NdH_x, Mg and Mg_2Ni/Ni small as long as possible.

Zhu *et al.*[21–23] reported the method of *in-situ* formation of $CeH_{2.73}$-MgH_2-Ni and YH_3-MgH_2-Mg_2NiH_4 nanocomposites through directly hydriding the $Mg_{80}Ce_{18}Ni_2$ and $Mg_{12}YNi$ alloys. They found that the composites of $CeH_{2.73}$-MgH_2-Ni remained its excellent performance after 500 H/D cycles because the *in-situ* formed nanocomposite structure suppressed the grain growth of Mg and MgH_2[21]. However, the as-melted $Mg_{80}Ce_{18}Ni_2$ alloy was a multiphase mixture which was composed of 57 wt.% $CeMg_3$, 29 wt.% Ce_2Mg_{17}, 7 wt.% CeMg, and 5 wt.% $CeMgNi_4$[21]. That is to say, the catalytic elements Ce and Ni didn't distribute uniformly in the alloy, which would lead to the non-uniformity of *in-situ* formed $CeH_{2.73}$-MgH_2-Ni composites. It is reasonable to assume that if the catalytic elements distribute uniformly in the whole alloy rather than concentrate in a few phases, the *in-situ* formed nanocomposites will become more homogenous. One of homogenous alloys is amorphous. Nanocrystallisation of the amorphous $LaMg_{11}Ni$ alloy led to the formation of Mg_2Ni/$Mg_{1.9}La_{0.1}Ni$ and $La_{1.8}Mg_{17}Ni_1$ nanocrystalline, which greatly improved the hydrogenation rate and lowered the temperature of hydrogen desorption[24,25]. Another easily available and stable alloy with homogenous microstructure is the single phase or intermetallic compound. Therefore, searching for the Mg-based multicomponent compound and synthesizing it with catalyst elements Nd and Ni are significant for *in-situ* formation of ultrafine NdH_x-MgH_2-Ni/Mg_2NiH_4 composites with excellent hydrogen storage properties. However, seeking for the Mg-based multicomponent compounds with good hydrogen storage properties is time-consuming through traditional trial-and-error method. A precise Nd-Mg-Ni phase diagram could help us to find a suitable target alloy for hydrogen storage and to select the reasonable process parameters for preparing it. The method combining the computational materials with the experimental verification would save a lot of time to explore new material.

Therefore, the purpose of this study is that how to explore the Nd-Mg-Ni hydrogen storage alloy with excellent properties for meeting the practical application by material design method in order to avoid the drawback of trial-and-error method, then the target alloy is prepared to verify validity. Moreover, the relationships between the thermodynamic property, kinetic performance and microstructure are systematically investigated in order to clarify the H/D mechanism. Specifically, through the first hydrogen-induced decomposition of the new ternary compound $Nd_4Mg_{80}Ni_8$, the nanocomposites of $NdH_{2.61}$-MgH_2-$Mg_2NiH_{0.3}$ are *in-situ* formed. This alloy shows fast H/D rates and good cycling behavior. The mechanism of hydrogen-induced decomposition and phase evolution during hydriding reaction are systematically analyzed by HR-TEM and *in-situ* SR-PXRD. Moreover, the kinetics mechanism is theoretically investigated by RPP model to clarify our experimental results.

Results and Discussions

The phase diagram of Nd-Mg-Ni system in Mg-rich corner at 400 °C.
The phase equilibria at 400 °C were determined by analyzing the phase composition of the four quenched samples. The XRD and EDS analysis of the alloys are listed in Table S1. In the Samples #1 and #2 annealed at 400 °C, an unknown phase (named as $Nd_4Mg_{80}Ni_8$) is observed with an average composition of at.% 4.86Nd-87.46Mg-7.68Ni, which is different from Nd_5Mg_{41}, Mg, Mg_2Ni and any other known ternary compounds. The morphology and XRD patterns of Sample #1 shown in Fig. 1(a,b) confirm the existence of the new ternary compound. The SEM images of Samples #2~4 in Fig. 1(c~e) show that the $Nd_4Mg_{80}Ni_8$ equilibrates with Mg, Mg_2Ni,
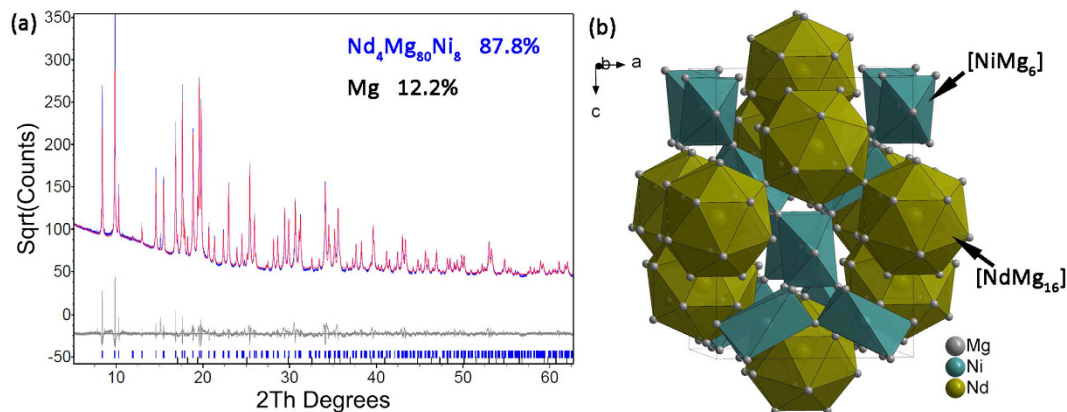
Figure 2. (**a**) The experimental (blue), fitted (red), and difference (grey line below observed and calculated patterns) SR-PXRD profiles for Sample #5 at a wavelength of 0.8262 Å and (**b**) the schematic crystal structure of $Nd_4Mg_{80}Ni_8$.

Formula sum	$Nd_4Mg_{80}Ni_8$
Formula weight	2990.88 g/mol
Crystal system	Tetragonal
Space group	$I\,4_1/a\,m\,d$ (No. 141)
Cell parameters	$a = b = 11.2743(1)$ Å, $c = 15.9170(2)$ Å
Cell volume	2023.19(4) Å^3
Z	4
Calc. density	2.45462 g/cm^3
R_{wp}	8.1%
R_B	6.4%
GoF	1.44

Table 1. Crystallographic data and structure refinement of $Nd_4Mg_{80}Ni_8$.

NdMg$_8$Ni and Nd$_5$Mg$_{41}$ phases. According to the experimental results, the determined phase diagram in the Mg-rich corner at 400 °C is plotted in Fig. 1(f).

The Nd-Mg-Ni ternary compounds are expected to be the hydrogen storage alloys with excellent properties because the uniform composition would leads to *in-situ* formation of the ultrafine MgH$_2$-NdH$_x$-Ni/ Mg$_2$NiH$_4$ composites[11,21,26]. From the reported literature and our experimental work, it can be found that there are seven ternary compounds in the Nd-Mg-Ni system: Nd$_4$Mg$_{80}$Ni$_8$, NdMg$_8$Ni, NdMg$_5$Ni$_2$[27], NdMg$_2$Ni[9], Nd$_2$MgNi$_2$[28], NdMgNi$_4$[29] and NdMg$_2$Ni$_9$[30]. The new compound Nd$_4$Mg$_{80}$Ni$_8$ is selected as the target alloy because of its highest content of Mg among those ternary compounds which indicates the maximum hydrogen capacity.

The crystal structure of $Nd_4Mg_{80}Ni_8$. In order to determine the crystal structure of Nd$_4$Mg$_{80}$Ni$_8$, the single phase was synthesized and examined by SR-PXRD. The actual composition of Sample #5 and #6 are Nd$_{4.08}$Mg$_{89.98}$Ni$_{5.94}$ and Nd$_{4.45}$Mg$_{84.64}$Ni$_{10.91}$, respectively. The SR-PXRD pattern of Sample #5 was indexed with a tetragonal unit cell using DICVOL06[31]. The structure solution started using the charge-flipping algorithm implemented in the program TOPAS v4.2[32]. The Ni and Nd atoms were easily located in the electron density maps. The structure was subsequently solved in the space group of $I4_1/amd$ (No. 141) by global optimization in direct space with 5 Mg atoms with no constraint using the program FOX[33]. Rietveld refinement was performed using TOPAS v4.2, and the refined lattice parameters were $a = b = 11.2743(1)$ Å, $c = 15.9170(2)$ Å, V = 2023.19(4) Å^3. The diffraction profile fitted by Rietveld refinement using these parameters is shown in Fig. 2(a), with the agreement factors of $R_{wp} = 8.1\%$, $R_B = 6.4\%$, and GoF = 1.44. The fitting result suggests that there were 87.8 wt.% Nd$_4$Mg$_{80}$Ni$_8$ and 12.2 wt.% Mg in the Sample #5. The details of the structure determination and crystallographic data are presented in Tables 1 and 2. The crystal structure of Nd$_4$Mg$_{80}$Ni$_8$ is shown in Fig. 2(b).

Nd$_4$Mg$_{80}$Ni$_8$ has a distinguished structure from other reported M-Mg-Ni (M = metal) ternary alloys. There is one symmetry independent Ni atom in the unit cell coordinates with six Mg atoms forming

Atoms	Wyck.	S.O.F	x/a	y/b	z/c	B iso (Å²)
Mg1	16h	1	0.13260	1/2	0.54657	1.865
Mg2	8d	1	0	1/4	5/8	1.865
Mg3	8e	1	1/2	1/2	5/8	1.865
Mg4	32i	1	0.36417	0.26792	0.31625	1.865
Mg5	16g	1	0.36383	0.63617	1/2	1.865
Ni1	8c	1	0	1/4	1/8	1.960
Nd1	4b	1	0	0	1/2	1.553

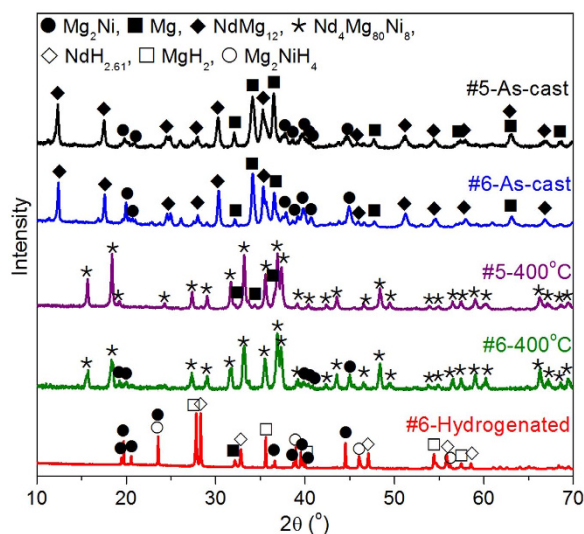**Table 2. The atomic parameters of $Nd_4Mg_{80}Ni_8$.**

Figure 3. The XRD patterns of $Nd_4Mg_{80}Ni_8$ with different heat treatment conditions.

[NiMg$_6$] in trigonal antiprism shape. Two different Ni-Nd bond distances are observed at 2.8186 and 2.8218 Å, which are close to the sum of the metallic radii $r_{Ni} + r_{Mg} = 2.85$ Å and larger than the sum of the covalent radii $r_{Ni} + r_{Mg} = 2.75$ Å[27]. While Nd atom in the unit cell coordinates with sixteen Mg atoms forming [NdMg$_{16}$], where Nd atom sits in the middle of tetrahexahedron with the Nd-Mg bond distances equaling to 3.4501, 3.5464 and 3.5660 Å. The shortest bond distance is slightly larger than the sum of the metallic radii 3.42 Å. The trigonal antiprisms of [NiMg$_6$] are linked together through vertices and the complex polyhedra of [NdMg$_{16}$] also linked together via shared vertices. Figure 2(b) shows both [NiMg$_6$] and [NdMg$_{16}$] complexes form two independent three-dimensional network in the structure.

The phase transformation of $Nd_4Mg_{80}Ni_8$ during as-cast → anneal → hydrogenation process. The XRD patterns of as-cast Sample #5 and #6 shown in Fig. 3 show that both of the samples are multiphase alloys containing NdMg$_{12}$, Mg and Mg$_2$Ni. NdMg$_{12}$ is a metastable phase in Nd-Mg system which forms if a nucleation barrier for Nd$_5$Mg$_{41}$ exists[34]. Therefore, the as-cast sample is not suitable for hydrogenation to *in-situ* form uniform nanocomposites of hydrides. According the established phase diagram, the equilibrated phase should be 90.7 wt.% Nd$_4$Mg$_{80}$Ni$_8$ with 9.3 wt.% Mg in Sample #5 and 88.3 wt.% Nd$_4$Mg$_{80}$Ni$_8$ with 11.7 wt.% Mg$_2$Ni in Sample #6 at 400 °C. In order to obtain a homogeneous alloy, both alloys were annealed at 400 °C for 2 days. It is found that NdMg$_{12}$ disappeared in the annealed samples and supplanted by Nd$_4$Mg$_{80}$Ni$_8$. The predicted phase fraction in Sample #5 is consistent with the result determined by SR-PXRD. Figure 3 shows the compared XRD patterns of the as-cast and annealed samples. A small amount of Mg$_2$Ni and Mg are still observed in the annealed samples due to the composition of prepared samples deviating from the designed value. On the other hand, it suggests that the solid solution range of Nd$_4$Mg$_{80}$Ni$_8$ is limited.

After Sample #6 powder is hydrogenated at 350 °C under 2.0 MPa H$_2$ for 1 h, the diffraction peaks of Nd$_4$Mg$_{80}$Ni$_8$ disappear and the pattern could be well indexed by NdH$_{2.61}$, MgH$_2$, Mg$_2$NiH$_{0.3}$, Mg$_2$NiH$_4$ and little Mg. Compared the XRD pattern of hydrogenated sample with that of the annealed, it can be seen that the overall amount of Mg$_2$Ni and Mg$_2$NiH$_4$ in hydrogenated sample is obviously larger than that in the annealed one. The evidence suggests that Nd$_4$Mg$_{80}$Ni$_8$ is decomposed to NdH$_{2.61}$, MgH$_2$, Mg$_2$NiH$_{0.3}$, Mg$_2$NiH$_4$ and Mg, because the elements Nd and Mg could only come from Nd$_4$Mg$_{80}$Ni$_8$. In
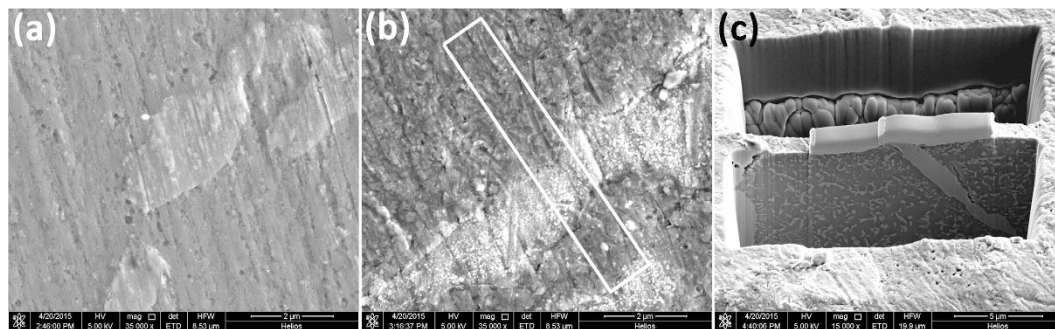
Figure 4. The microstructure of $Nd_4Mg_{80}Ni_8$: (**a**) before hydrogenation, (**b**) after hydriding at 350 °C for 1 h, and (**c**) the vertical section of hydrogenated sample.

order to make sure whether $NdH_{2.61}$, MgH_2 and Mg_2NiH_4 are formed *in-situ* or not and understand the hydrogen-induced decomposition mechanism of $Nd_4Mg_{80}Ni_8$, the microstructure and phase composition of the incompletely hydrogenated bulk Sample #5 was investigated by HR-TEM.

The mechanism of hydrogen-induced decomposition and the formation of $NdH_{2.61}$-MgH_2-$Mg_2NiH_{0.3}$ nanocomposites.
The comparison of the microstructure of $Nd_4Mg_{80}Ni_8$ and incompletely hydrogenated sample is shown in Fig. 4. The starting material shows plate-like Mg_2Ni in the $Nd_4Mg_{80}Ni_8$ matrix. After hydrogenation the surface of $Nd_4Mg_{80}Ni_8$ becomes rough. Many ultrafine white particles are observed on the Mg_2Ni. The original $Nd_4Mg_{80}Ni_8$/Mg_2Ni phase boundaries in the starting alloy are still visible. By excavating holes on the hydrogenated sample, the inner microstructure is shown in Fig. 4(c). Many second phases precipitate from the $Nd_4Mg_{80}Ni_8$ matrix after hydrogenation.

HR-TEM was used to determine the phase composition and analyze the microstructure evolution during hydrogenation. The bright-field image, selected area electron diffraction (SAED) pattern and HR-TEM image of the $Nd_4Mg_{80}Ni_8$ are shown in Fig. 5 (a~c). The composition of the selected area agrees well with the nominal composition of $Nd_4Mg_{80}Ni_8$. The indexing of SAED pattern is consistent with the result of SR-PXRD. In addition, a weak polycrystalline diffraction ring is observed with interplanar spacing $d = 2.105$ Å which corresponds to the crystal plane of (110) of Nd_2O_3 ($d = 1.9735$ Å). It indicates that a little Nd_2O_3 formed on the surface of the thin slice. From the aspect of thermodynamics, the oxide of Nd should form earlier than the oxide of Mg and Ni because of the lower Gibbs free energy of formation of Nd oxide. The interplanar spacing of d_1 and d_2 in Fig. 5(c) correspond to the crystal planes of $(1\bar{1}2)$ and $(21\bar{1})$ of $Nd_4Mg_{80}Ni_8$. Both values agree with 5.6323 Å and 4.8066 Å determined by SR-PXRD with relative error of 1.36% and 1.80%, respectively. The HR-TEM image shows that the $Nd_4Mg_{80}Ni_8$ compound is homogeneous and highly crystallized.

Figure 5(d) shows the bright field image of the incompletely hydrogenated sample. The plate-like Mg_2Ni in starting alloy dissolves little hydrogen to become the solid solution of $Mg_2NiH_{0.3}$, which is identified by the SAED pattern given in Fig. 5(e). The composition of the $Mg_2NiH_{0.3}$ at the position marked by yellow point is at.% 0.46Nd-66.05Mg-33.49Ni. The hydrogen cannot be detected from EDS. From Fig. 5(d), an original grain boundary in the starting alloy of $Nd_4Mg_{80}Ni_8$ is observed. Many fine equiaxed dark particles with size in the range of 58~250 nm distributed randomly in the bright matrix.

Figure 5(f) shows the magnified TEM image of the region which was single phase $Nd_4Mg_{80}Ni_8$ in starting material. From Fig. 5(g), it can be seen that numerous ultrafine particles distribute in both bright and dark phases. The composition of dark phase is at.% 4.47Nd-71.78Mg-23.76Ni. It is $Mg_2NiH_{0.3}$ which is identified by SAED pattern shown in Fig. 5(g). The index of the diffraction rings indicates that the high density particles in $Mg_2NiH_{0.3}$ are $NdH_{2.61}$ nanoparticles. The high content of 4.47 at.% Nd on the $Mg_2NiH_{0.3}$ is contributed by the $NdH_{2.61}$. Figure 5(h) shows the high resolution TEM image of the region marked as blue frame in Fig. 5(g). The interplanar spacing of the bright matrix is $d = 2.250$ Å which corresponds to the crystal plane (110) of MgH_2 ($d = 2.2570$ Å). Numerous equiaxed grains of $NdH_{2.61}$ are distributed in the matrix MgH_2. The average composition of bright region is at.% 5.70Nd-93.23Mg-1.07Ni. The difference of Nd content in $Mg_2NiH_{0.3}$ and MgH_2 phases is small, which also indicates that the $NdH_{2.61}$ particles distribute uniformly in both MgH_2 and $Mg_2NiH_{0.3}$ phases. The $NdH_{2.61}$ is nanocrystalline with grain size of about 4~40 nm. Figure 5(i) gives the composition map of Nd, Mg and Ni. It shows that the Nd element concentrates in the nanoparticles and Ni element concentrates in $Mg_2NiH_{0.3}$ phases.

Based on the TEM results, the mechanism of hydrogen-induced microstructure evolution can be revealed. When the alloy reacts with hydrogen, the Nd atoms firstly disassociate from $Nd_4Mg_{80}Ni_8$ to generate $NdH_{2.61}$ because the enthalpy of formation of $NdH_{2.61}$ ($-207.2 \sim -187.6$ kJ/mol[35,36]) is relatively lower than that of MgH_2 and Mg_2NiH_4. After the ultrafine nanoparticles of $NdH_{2.61}$ *in-situ* generating from the original $Nd_4Mg_{80}Ni_8$ compound, the structure of $Nd_4Mg_{80}Ni_8$ becomes unstable because the
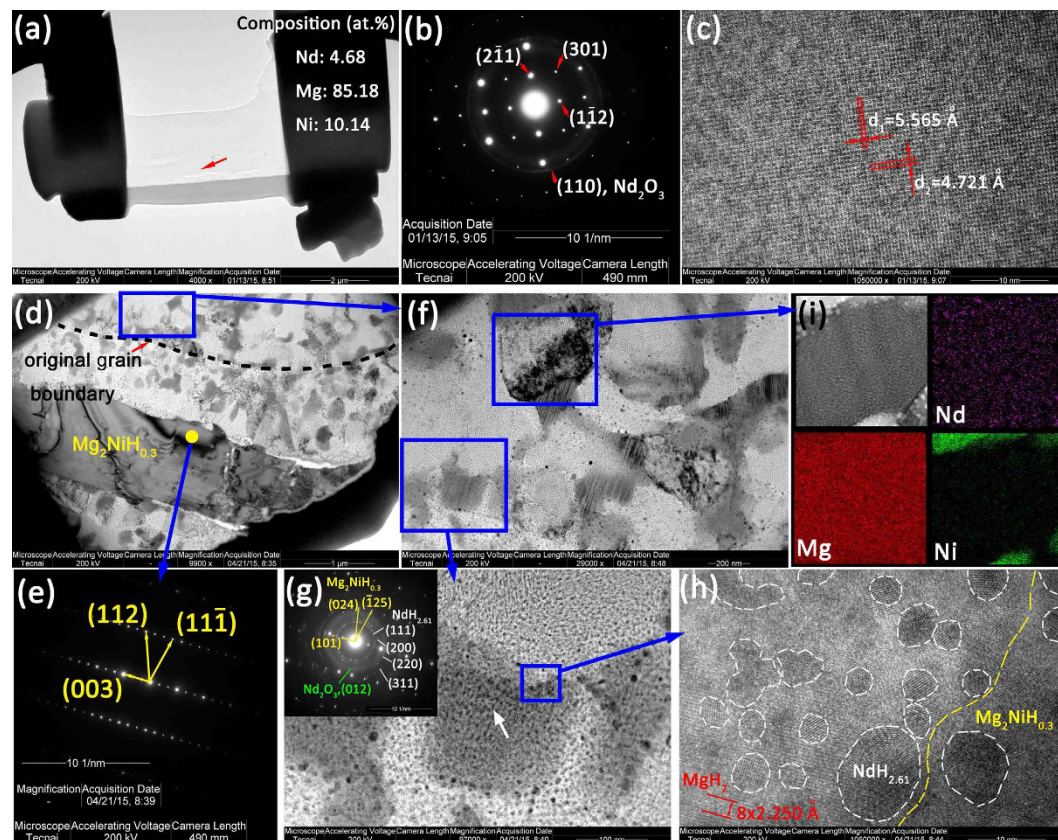
Figure 5. (**a**) The TEM bright-field image of $Nd_4Mg_{80}Ni_8$, (**b**) the SAED pattern of $Nd_4Mg_{80}Ni_8$, (**c**) HR-TEM image of $Nd_4Mg_{80}Ni_8$, (**d**) the bright field image of incompletely hydrogenated Sample #6, (**e**) SAED pattern of $Mg_2NiH_{0.3}$, (**f**) the magnified image of the incompletely hydrogenated $Nd_4Mg_{80}Ni_8$, (**g**) the magnified image of MgH_2 and $Mg_2NiH_{0.3}$ and the SAED pattern of dark phase, (**h**) the HR-TEM image of $MgH_2/Mg_2NiH_{0.3}$ interface, and (**i**) the composition map of Nd, Mg and Ni.

absence of Nd atoms leads to the polyhedra of $[NdMg_{16}]$ crumbling. The released Mg atoms make the structure highly disorder. According to the equilibrated phase diagram, the rest composition will shift to $Mg + Mg_2Ni$ two-phase region. The Mg and Ni atoms diffuse fast owing to the disordered structure. Then large particles of Mg and Mg_2Ni (58~250 nm) form to reduce the Gibbs free energy of system. After the $Nd_4Mg_{80}Ni_8$ transforming to $NdH_{2.61}$-Mg-Mg_2Ni nanocomposites, the Mg reacts with hydrogen to generate MgH_2 and the hydrogen atoms dissolve in Mg_2Ni to generate $Mg_2NiH_{0.3}$. The high density $NdH_{2.61}$ nanoparticles, numerous interfaces between MgH_2 and $Mg_2NiH_{0.3}$, and a large number of grain boundaries in the nanocomposites of $NdH_{2.61}$-Mg-Mg_2Ni may provide a great deal of hydrogen atoms diffusion channels and nucleation sites of hydrides. Thus, the $NdH_{2.61}$-MgH_2-$Mg_2NiH_{0.3}$ nanocomposites should exhibit excellent H/D kinetics.

The thermodynamic and kinetic properties of H/D reactions in $Nd_4Mg_{80}Ni_8$. The Sample #6 shows a good activation behavior at 350 °C. At the second H/D cycle, it reaches a maximum hydrogen capacity of 5.15 wt.% which is near to the theoretical value 5.18 wt.% H_2. All the PCT curves at different temperatures shown in Fig. 6(a) manifests two flat plateaus, indicating that there are two phases reacting with hydrogen during the H/D processes. One of phases exhibits larger storage capacity and wider plateau of H/D reactions marked as the first plateau in Fig. 6(a). The second phase shows higher equilibrium pressure of hydrogen and narrower plateau marked as the second plateau. Table 3 gives plateau pressures, maximum hydrogen capacities at different temperatures and thermodynamic data for the different phases. The hysteresis factor defined as $Hf = \ln(P_{ab}/P_{de})$ are 0.144, 0.206 and 0.134 at 350, 300 and 250 °C respectively for the first plateau and 0.474, 0.693 and 1.366 for the second plateau. The enthalpies and entropies are derived from the Van't Hoff equation. The enthalpies of H/D reactions for the first phase are consistent with the reported values of MgH_2 in the range of 71.9~78.0 kJ/mol[8,17,21,37]. The enthalpies of H/D reactions for the second phase are consistent with the reported values of Mg_2NiH_4 in the range of 53.23~72.9 kJ/mol[38–43]. The comparison indicates that both thermodynamic properties of MgH_2 and Mg_2NiH_4 are basically unchanged by adding 4.5 at.% $NdH_{2.61}$.
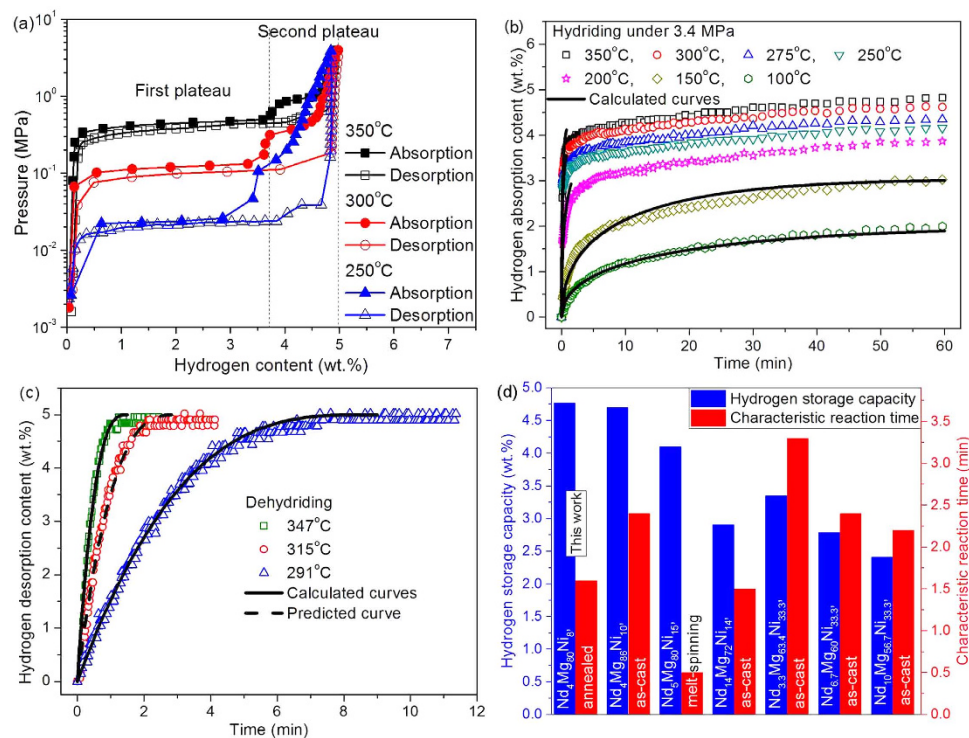
Figure 6. (**a**) The PCT curves of $Nd_4Mg_{80}Ni_8$ at 250, 300 and 350 °C, (**b**) the absorption kinetic curves in the temperature range of $100 \sim 350$ °C, (**c**) the desorption kinetic curves at 291, 315 and 347 °C, and (**d**) the comparison of hydrogen storage capacity and hydriding rate for Nd-Mg-Ni alloys at 300 °C.

Plateau	T (°C)	P_{ab} (MPa)	P_{de} (MPa)	C_{ab} (wt.%)	Calculated ΔH (kJ/mol) and ΔS (J/(mol·K))	
					Absorption	Desorption
First plateau (0 ~ 3.74wt.%H)	350	0.441	0.382	3.74	$\Delta H = -79.1 \pm 0.5$	$\Delta H = 784 \pm 1.9$
	300	0.118	0.096	3.62	$\Delta S = -120.3 \pm 0.8$	$\Delta S = 117.6 \pm 3.3$
	250	0.024	0.021	3.41		
Second plateau (3.74 ~ 4.94wt.%H)	350	0.908	0.565	1.20	$\Delta H = -48.8 \pm 2.5$	$\Delta H = 727 \pm 3.2$
	300	0.368	0.184	1.36	$\Delta S = -77.3 \pm 4.3$	$\Delta S = 112.3 \pm 5.6$
	250	0.149	0.038	1.43		

Table 3. The H/D properties and thermodynamic data of $Nd_4Mg_{80}Ni_8$. Note: P_{ab} and P_{de} are H/D plateau pressures, C_{ab} is capacities of hydrogen absorption.

Figure 6(b) shows the hydriding behavior of $Nd_4Mg_{80}Ni_8$ in the temperature range from 100 to 350 °C. It absorbs 85% of the maximum hydrogen content above 250 °C within 5.8 min. After that the hydrogen absorption content increases slowly with prolonging time. At 1 h, the alloy absorbs 4.82 wt.% hydrogen at 350 °C, which is 93% of the theoretical hydrogen storage content. The sample exhibits good desorption kinetics as shown in Fig. 6(c). It releases the absorbed hydrogen thoroughly within 8.3 min when the sample is heated up to 291 °C.

Lots of scholars developed kinetic models for the gas-solid reaction, such as Jander model[44], Ginstling-Brounshtein equation[45], etc. Evard *et al.*[46] developed a mathematical model to describe the non-isothermal decomposition process of MgH_2, which took into account relative rates of hydrogen desorption, chemical transformation on the MgH_2-Mg interface and size distribution of the powder particles. In our previous work, Chou *et al.*[47–49] proposed a series of formulae concerning the isothermal kinetics of gas-solid reaction based on a real physical picture. All parameters in RPP model have clear physical meanings and the effects of temperature, pressure, particle size, sample shape, density change of resultant on the reaction fraction can be analyzed quantitatively. The treatment of this model avoids the multistep calculation error at multi-temperatures and multi-pressures[50]. up to now, the RPP model has

been successfully used in analyzing the H/D kinetics of Mg-Ni alloy[50–52], LaNi$_5$-based alloy[9], Mg-LaNi$_5$[53], La$_2$Mg$_{17}$-based composites[54], etc. Therefore, the isothermal H/D kinetics of the Nd$_4$Mg$_{80}$Ni$_8$ are analyzed by fitting the observed curves using the RPP model. It is found that the rate controlling step is the diffusion of hydrogen in the hydride during hydrogenation by fitting the experimental data with Eq. (5).

$$\xi = 1 - \left(1 - \sqrt{\frac{t}{t_{c(d)}}}\right)^3$$

(1)

where

$$t_{c(d)} = \frac{R_0^2 \rho}{2MD_H^0 K_d \left(\sqrt{P_{H_2}} - \sqrt{P_{eq}}\right) \exp\left(-\frac{\Delta E}{RT}\right)}$$

(2)

ξ the reacted fraction equaling to the ratio of hydrogen absorption weight Δm at time t to the maximum hydrogen absorption weight Δm_{max}, $t_{c(d)}$ the characteristic reaction time representing the required time of a completely hydriding or dehydriding of the sample, P_{H2} the partial pressure of hydrogen in gas phase, P_{eq} the hydrogen partial pressure in equilibrium with hydride, and ΔE the activation energy. The characteristic time t_c is regarded as a criterion for reaction rate: the larger the characteristic time, the slower the reaction rate. The corresponding squared correlation coefficient, r^2, reflects the level of agreement between fitting curve and experimental data. Using Eq. (1) to fit the hydrogenation data, the calculated $t_{c(d)}$ decreases from 153.5 to 1.6 min when temperature increases from 100 to 300 °C, indicating that the hydriding reaction rate increases with the temperature rising. The apparent activation energy for hydrogenation is determined to be 82.3 kJ/mol by fitting the experimental data using Eq. (2).

There is an interesting phenomenon that the fastest hydriding rate is observed at 300 °C for Nd$_4$Mg$_{80}$Ni$_8$ ($t_{c(d)} = 1.6$ min) alloy within the investigated temperature range from 100 to 350 °C. It is known that both the forward reaction rate (hydriding reaction) and reverse reaction rate (dehydriding reaction) are accelerated with the increasing temperature. In addition, the hydrogenation of Mg and Mg$_2$Ni is exothermic, while the dehydrogenation reaction is endothermic. The increase of temperature is propitious for the reverse reaction. If the reverse reaction rate increases more rapidly than the forward reaction rate, an apparent fastest hydriding rate would be found in the temperature range.

In order to compare the hydriding rate of Nd$_4$Mg$_{80}$Ni$_8$ with that of other Nd-Mg-Ni alloys in literatures[12,13,16,18,26], the calculated results of characteristic reaction time are listed in Table S2. Figure 6(d) shows the comparison of hydrogen storage capacity and hydriding rate of those alloys at 300 °C. Except the samples prepared by melt-spinning, the fastest two hydrogenation are observed from Nd$_{14}$Mg$_{72}$Ni$_{14}$ ($t_{c(d)} = 1.5$ min) and Nd$_4$Mg$_{80}$Ni$_8$ ($t_{c(d)} = 1.6$ min) alloys at 300 °C. However, the maximum hydrogen absorption content of Nd$_{14}$Mg$_{72}$Ni$_{14}$ is only 2.91 wt.%, relatively smaller than that of Nd$_4$Mg$_{80}$Ni$_8$ (4.77 wt.%) at the same temperature. The composition of as-cast Nd$_4$Mg$_{86}$Ni$_{10}$ alloy[13] is very close to Nd$_4$Mg$_{80}$Ni$_8$ developed in present work, but the as-cast Nd$_4$Mg$_{86}$Ni$_{10}$ is a multiphase alloy consisted of NdMg$_{12}$, Mg and Mg$_2$Ni phases. This indicates that the composition distribution in the annealed Nd$_4$Mg$_{80}$Ni$_8$ is more uniform than that in as-cast Nd$_4$Mg$_{86}$Ni$_{10}$, which results in that the *in-situ* formed NdH$_{2.61}$-Mg-Mg$_2$Ni nanocomposites more homogenous than that in as-cast Nd$_4$Mg$_{86}$Ni$_{10}$. As calculated from RPP model, the characteristic hydriding time at 300 °C for Nd$_5$Mg$_{80}$Ni$_{15}$ ([12], 3.5 MPa), Nd$_4$Mg$_{80}$Ni$_8$ (this work, 3.4 MPa) and Nd$_4$Mg$_{86}$Ni$_{10}$ ([13], 3.0 MPa) are 0.5, 1.6 and 4.7 min, respectively. It indicated that the hydriding rate of Nd$_5$Mg$_{80}$Ni$_{15}$ alloy is the fastest, while the hydriding rate of Nd$_4$Mg$_{86}$Ni$_{10}$ is much slower than that of the other two alloys. The hydriding rate is related to many factors, such as temperature, hydrogen pressure, microstructure, powder size, composition, etc. Both of Nd$_5$Mg$_{80}$Ni$_{15}$ and Nd$_4$Mg$_{80}$Ni$_8$ using for hydriding are nanocrystalline structure, but the particle size of Nd$_5$Mg$_{80}$Ni$_{15}$ is much smaller than the micro-particles of Nd$_4$Mg$_{80}$Ni$_8$ (-100 mesh) and Nd$_4$Mg$_{86}$Ni$_{10}$ (~ 70 mesh). The smaller the sample size, the faster the hydriding rate. In addition, the Ni content in Nd$_5$Mg$_{80}$Ni$_{15}$ is higher than that in Nd$_4$Mg$_{80}$Ni$_8$ and Nd$_4$Mg$_{86}$Ni$_{10}$, which means the quantity of catalytic element is more than Nd$_4$Mg$_{80}$Ni$_8$ and Nd$_4$Mg$_{86}$Ni$_{10}$. Therefore, the hydriding rate of melt-spinning and crystallized Nd$_5$Mg$_{80}$Ni$_{15}$ showed better hydriding kinetics than that of Nd$_4$Mg$_{80}$Ni$_8$ and Nd$_4$Mg$_{86}$Ni$_{10}$. But the increase of Ni content reduced the hydrogen storage capacity (Nd$_5$Mg$_{80}$Ni$_{15}$: 4.10 wt.%, Nd$_4$Mg$_{80}$Ni$_8$: 4.77 wt.%, and Nd$_4$Mg$_{86}$Ni$_{10}$: 4.70 wt.%). The comparison of all alloys in Fig. 6(d) shows that the optimal Nd-Mg-Ni alloy is the Nd$_4$Mg$_{80}$Ni$_8$ designed in present work by considering the hydriding kinetics and hydrogen storage capacity.

The rate controlling steps are surface penetration (sp) of hydrogen atoms for dehydriding reaction at 291 ∼ 347 °C through fitting the experimental data with Eq. (7).

$$\xi = 1 - \left(1 - \frac{t}{t_{c(sp)}}\right)^3$$

(3)

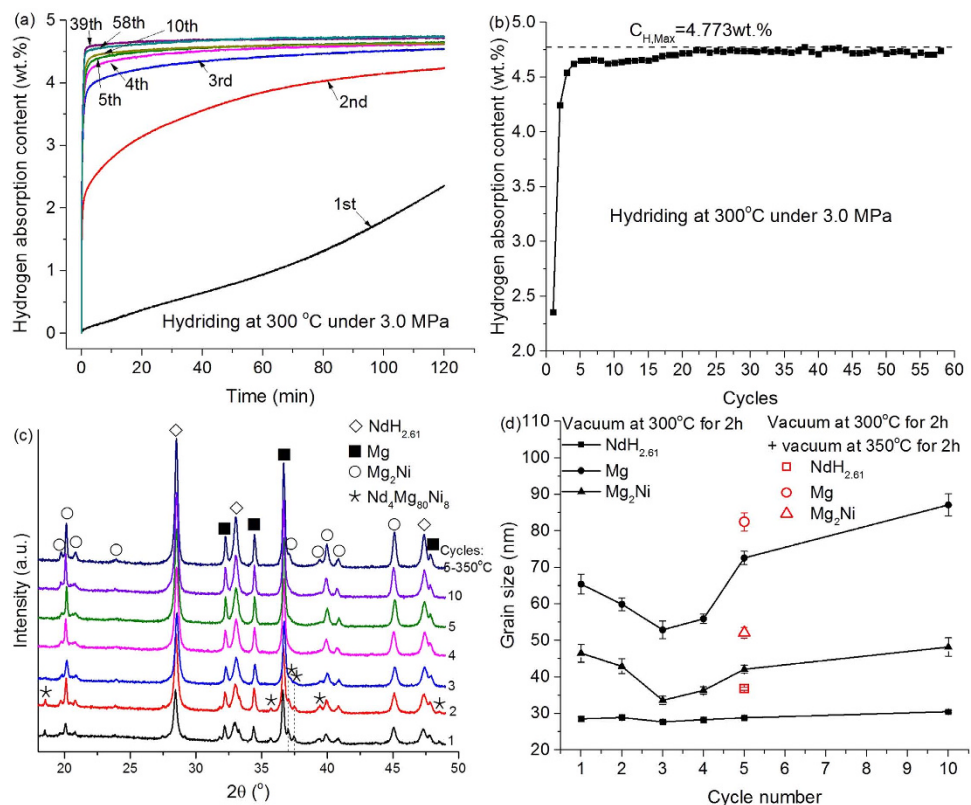**Figure 7.** (**a**) The hydriding behavior of $Nd_4Mg_{80}Ni_8$ at 300 °C under 3.0 MPa H_2 at different cycles, (**b**) the hydrogen storage capacity versus cycle times, (**c**) the XRD patterns of completely dehydrogenated samples after different cycles, and (**d**) the relationship between grain size and cycle number.

where

$$t_{c\,(sp)} = \frac{R_0 \rho}{K_{sp}\left(\sqrt{P_H} - \sqrt{P_{eq}}\right)\exp\left(-\frac{\Delta E}{RT}\right)} \tag{4}$$

The calculated $t_{c(sp)}$ are 8.8, 3.0 and 1.5 min with temperature increasing from 291 to 347 °C. This means that the dehydriding reaction rate increases with the temperature rising. The activation energy for dehydrogenation is calculated to be 97.5 kJ/mol, which is much smaller than 160 kJ/mol for ball milled pure MgH_2[55], 124.6 kJ/mol for induction melted $Mg_{90}Ce_5Ni_5$ alloy[8], and comparable to 104 kJ/mol for the as-cast $CeMg_3$[21]. Combining Eqs (3 and 4), the dehydriding kinetic curves at any other temperatures can be predicted by RPP model as follows:

$$\Delta m = 5.0wt.\,\% \times \left[1 - \left(1 - \frac{\exp\left(-\frac{97500}{RT}\right)}{7.9439 \times 10^{-9}} \cdot t\right)^3\right] \tag{5}$$

where R the gas constant, T temperature in Kelvin, and 5.0 wt.% the largest desorption hydrogen content from experimental. The calculated and predicted curves are shown in Fig. 6(c), which suggests that the theoretical calculation agree well with experimental data.

The cycle life kinetics was examined at 300 °C under 3.0 MPa H_2. The hydriding behaviors of the 1st ~ 5th, 10th, 39th and 58th cycles are showed in Fig. 7(a). It can be seen that the hydriding rate increases with the increase of cycle times from 1st to 5th. After the 5th cycle, the hydriding rate becomes very fast. Figure 7(b) shows the hydrogen storage capacity versus cycle times. The hydrogen capacity increases sharply from 2.36 to 4.54 wt.% in the first 3 cycles and then increases gradually to the maximum value of 4.77 wt.%. Until the 58th cycle, the hydrogen storage capacity still remains stable, which suggests that the $Nd_4Mg_{80}Ni_8$ has a good cycle ability. In order to investigate the relationship between grain size and cycle times, the XRD pattern was collected after the 1st ~ 5th and 10th cycles, shown in Fig. 7(c). The samples were vacuumed at 300 °C for 2 h. A part of powders after the 5th cycle were further vacuumed at 350 °C for 2 h.
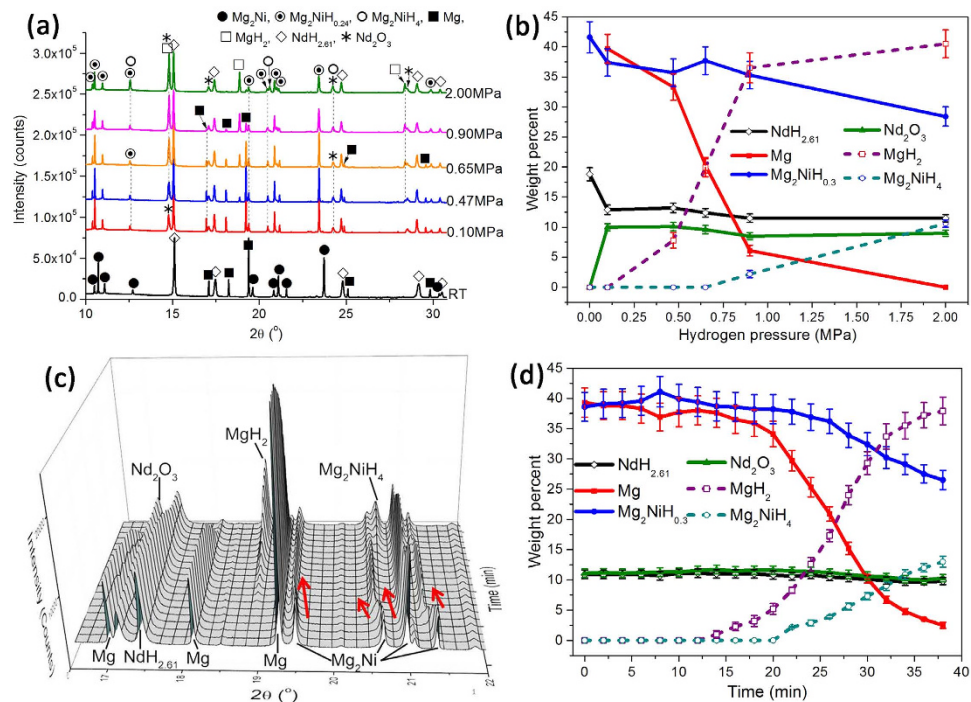
Figure 8. (**a**) The SR-PXRD patterns of $NdH_{2.61}$-Mg-Mg_2Ni composites under different hydrogen pressures at 350 °C, (**b**) the weight fraction of each phase versus pressure, (**c**) the SR-PXRD patterns of $NdH_{2.61}$-Mg-Mg_2Ni composites during hydriding process at different time at 300 °C, and (**d**) the weight fraction of each phase versus time.
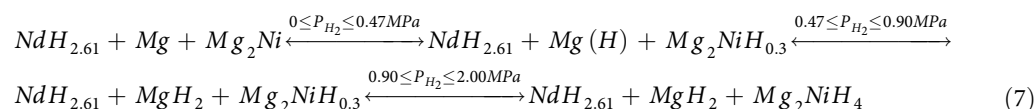
The calculated grain size versus cycle numbers is showed in Fig. 7(d). It can be seen that the grain size of $NdH_{2.61}$ increase slowly with the cycle number, but the grain sizes of Mg and Mg_2Ni decrease in the first 3 cycles and then increase with the increase of cycle number. The $Nd_4Mg_{80}Ni_8$ disappears until the 4th cycle and the phase fractions of $Nd_4Mg_{80}Ni_8$ in the first 3 cycles are 7.0 ± 0.6, 4.1 ± 0.2 and 2.5 ± 0.5 wt.%, respectively. Although most of $Nd_4Mg_{80}Ni_8$ decomposed in the 1st cycle, the hydrogen absorption content is only 2.36wt.%. It suggests the generated Mg and Mg_2Ni didn't absorb hydrogen fully. Therefore, in the 2nd and 3rd cycle, the uncompleted phase transformation of $Mg \leftrightarrow MgH_2$ and $Mg_2Ni \leftrightarrow Mg_2NiH_4$ reduced the grain size of Mg and Mg_2Ni. After the sample is completely activated, the phase transformation can be finished at the initial stage of H/D process. The long holding time at this temperature leads to the growth of grain size. Therefore, after the 4th cycle the grain sizes of Mg and Mg_2Ni growth obviously.

The grain size of the sample further vacuumed at 350 °C is larger than that dehydriding at 300 °C. It suggests that the grain size grows with the raise of temperature and the extension of time. The growth of $NdH_{2.61}$ is slowly with cycle times, but the growth of Mg is obviously from 60 ± 2 nm after the 3rd cycle to 87 ± 3 nm after the 10th cycle. The grain size of Mg vacuumed at 350 °C is about 83 ± 3 nm which is smaller than the value of Mg (150 nm) reported by Denys et al.[20] at the same temperature. This is because it was pure Mg sample used in their study, while the well-distributed $NdH_{2.61}$ and Mg_2Ni in present work can restrain the growth of Mg[21].

The phase transformation of $NdH_{2.61}$-Mg-Mg_2Ni nanocomposites during hydrogenation. The phase evolution mechanism of RE-Mg-Ni alloys during hydrogenation/dehydrogenation process was well clarified by Denys et al.[20,24,25] combining in-situ SR-PXRD. The effect of solidification rate on the microstructure of alloy, phase structural and microstructural state of constituents during reversible process of synthesis and decomposition of hydrides, and kinetic mechanism during hydriding and dehydriding process were studied in detail. Inspiring by their work, the in-situ SR-PXRD assisted with Rietveld refinement was also applied to study the mechanism of phase transformation under different hydrogen pressures and at different time. The SR-PXRD patterns under different hydrogen pressures at 350 °C are shown in Fig. 8(a). The indexation of the pattern of the activated powders indicates the existence of $NdH_{2.61}$, MgH_2 and Mg_2Ni. Combined with the TEM results, the reaction taking place during the first hydrogenation is assumed to be:

$$Nd_4Mg_{80}Ni_8 + 85.22H_2 \rightarrow 4NdH_{2.61} + 64MgH_2 + 8Mg_2NiH_4 \qquad (6)$$
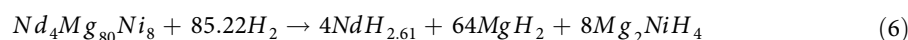
The calculated fraction of each phase versus pressure is plotted in Fig. 8(b). The sample of complete dehydrogenation contained 18.8 wt.% $NdH_{2.61}$, 39.5 wt.% Mg and remainder Mg_2Ni. As temperature increased to 350 °C under 0.10 MPa H_2, the phase fraction of Mg and Mg_2Ni didn't change. However, 10.0 wt.% Nd_2O_3 emerged because of the oxidation of $NdH_{2.61}$ during heating process. Then the content of Nd_2O_3 remained stable at this level under hydrogen atmosphere. 0.47 MPa H_2 is close to the pressure of the lower flat plateau at 350 °C. It is found that 7.8 wt.% MgH_2 appeared and the fraction of Mg reduced to 33.3 wt.%. The result indicates that the flat plateau at 0.47 MPa H_2 corresponds to the phase equilibrium of $Mg + MgH_2 + NdH_{2.61} + Mg_2NiH_{0.3}$. The hydrogen absorption content of 0.15 wt.% H_2 before the lower flat plateau is contributed by the solid solution of hydrogen in Mg and $Mg_2NiH_{0.3}$. When the Mg transforms to MgH_2 entirely, the hydrogen absorption content reaches to 3.74 wt.% (As shown in Fig.6 (a)). The Mg_2NiH_4 doesn't emerge until hydrogen pressure increases to 0.90 MPa. The second flat plateau corresponds to the equilibrium of $Mg_2NiH_{0.3} + Mg_2NiH_4 + MgH_2 + NdH_{2.61}$. At 2.00 MPa H_2, the Mg is depleted, but 28.4 wt.% $Mg_2NiH_{0.3}$ (the solid solution of hydrogen) is remained because of the alloy doesn't reach the equilibrium state during the measurement. Based on those results, the sequence of the phase transformations with equilibrium hydrogen pressure during hydrogenation at 350 °C is presented as follows:

$$NdH_{2.61} + Mg + Mg_2Ni \xleftrightarrow{0 \leq P_{H_2} \leq 0.47MPa} NdH_{2.61} + Mg\,(H) + Mg_2NiH_{0.3} \xleftrightarrow{0.47 \leq P_{H_2} \leq 0.90MPa}$$

$$NdH_{2.61} + MgH_2 + Mg_2NiH_{0.3} \xleftrightarrow{0.90 \leq P_{H_2} \leq 2.00MPa} NdH_{2.61} + MgH_2 + Mg_2NiH_4 \qquad (7)$$

Seen from the isothermal hydriding kinetic curves as shown in Fig. 6(b), the hydriding process of the alloy above 200 °C can be separated as two stages. The first was the rapid hydriding stage, while the second stage exhibited relatively slow hydriding rate. The phase composition during the hydriding process at 300 °C under 2.00 MPa H_2 was analyzed by *in-situ* SR-PXRD, shown in Fig. 8(c). The Mg_2Ni phase peaks shifts left toward lower 2θ values as time increases to 8 min (marked as the red arrows) which suggests the lattice expansion of the Mg_2Ni phase causing by the solid solution of hydrogen atoms. The intensity of Mg and Mg_2Ni decreases with time prolonging, indicating the Mg and Mg_2Ni transforms to MgH_2 and Mg_2NiH_4, respectively. The change of phase fractions refined by Rietveld method is plotted in Fig. 8(d). About 11.3 wt.% Nd_2O_3 emerges and doesn't change significantly later. There is no hydride appearing until 14 min. The delay of the hydrogenation may be due to the slight oxidation of the powders during heating process. The MgH_2 appeared earlier than Mg_2NiH_4 and its fraction increases with the prolongation of time. At 40 min, the Mg transforms into MgH_2 almost completely, but 26.5 wt.% $Mg_2NiH_{0.3}$ is left. The hydrogen absorption process of $Mg_8Mm_{20}Ni$ alloy identified by Denys *et al.*[20] was as following sequence: (1) $Mg_2Ni \rightarrow Mg_2NiH_{0.3}$, (2) $MmH_2 \rightarrow MmH_3$ and $Mg \rightarrow MgH_2$, and (3) $Mg_2NiH_{0.3} \rightarrow Mg_2NiH_4$. They thought that the transformation of $Mg_2Ni \rightarrow Mg_2NiH_{0.3}$ occurred earlier than other transformations is because the instantly formed α-solid solution $Mg_2NiH_{0.3}$ catalyzed the hydrogenation of Mg. Therefore, one can believe that the fast hydriding rate of the first stage results from the fast hydrogenation of Mg.

In summary, the isothermal section of Nd-Mg-Ni system in the Mg-rich corner at 400 °C was established based on the phase relationships determined from equilibrated alloys. A new ternary compound $Nd_4Mg_{80}Ni_8$ was found and it exhibited excellent H/D kinetic properties as a novel hydrogen storage alloy. It has structure of space group $I4_1/amd$ (No.142), Z = 4, $a = b = 11.2743(1)$ Å, $c = 15.9170(2)$ Å. HR-TEM results revealed that the hydrogen-induced decomposition of $Nd_4Mg_{80}Ni_8$ lead to *in-situ* formation of $NdH_{2.61}$-MgH_2-$Mg_2NiH_{0.3}$ nanocomposites. The high density grain boundaries in the nanocomposites of $NdH_{2.61}$-Mg-Mg_2Ni provided a great deal of hydrogen atoms diffusion channels and nucleation sites of hydrides, which greatly enhances the H/D kinetics and improved the cycle ability. The grain size of $NdH_{2.61}$ grows slowly with cycle number, but the grain sizes of Mg and Mg_2Ni decrease in the first 3 cycles, and then increase with the increase of cycle times. The growth of grain size is related with temperature and vacuum time. The kinetics mechanism is analyzed by RPP model, which suggests that the rate controlling step was diffusion for hydrogenation and surface penetration for dehydrogenation. The *in-situ* SR-PXRD results revealed that the sequence of phase transformation during hydrogenation at 350 °C was $NdH_{2.61} + Mg + Mg_2Ni \rightarrow NdH_{2.61} + Mg(H) + Mg_2NiH_{0.3} \rightarrow NdH_{2.61} + MgH_2 + Mg_2NiH_{0.3} \rightarrow NdH_{2.61} + MgH_2 + Mg_2NiH_4$ with the increase of equilibrium hydrogen pressure from 0.0 to 2.0 MPa. Mg absorbed hydrogen earlier and faster than Mg_2Ni during isothermal hydrogenation at 300 °C under 2.0 MPa H_2.

Experimental Methods

The preparation and examination of the equilibrated alloys.
The Nd-Mg-Ni samples were prepared by a medium frequency induction furnace using blocks of Nd (≥99.99 wt.%), Mg (≥99.99 wt.%) and Ni (≥99.99 wt.%) as the starting materials. The as-cast samples were enclosed by tantalum foils for subsequently sealing in evacuated quartz tubes. The samples were annealed at 400 °C for 30 days and then quenched in ice-water. The sample compositions and heat treatment conditions were listed in Table S1.

The actual composition of each alloy was determined by inductively coupled plasma atomic emission spectrometry (ICP). The microstructure and composition of phases in the bulk samples were investigated by HITACHI SU-1500 scanning electron microscopy (SEM) equipped with energy dispersive X-ray

spectrometer (EDS). The phase composition of annealed samples were characterized by X-ray diffraction (XRD) using 18KW D/MAX2500V + /PC diffractometer with Cu Kα radiation.

The solution of crystal structure. According to the average composition of at.% 4.86Nd-87.46Mg-7.68Ni detected from EDS, the $Nd_4Mg_{80}Ni_8$ compound (Sample #5) was prepared by annealing an induction melted ingot at 400°C for 30 days followed by ice-water quenching. The actual composition determined by ICP located in the region of $Nd_4Mg_{80}Ni_8 + Mg$ two-phase equilibrium. SR-PXRD data for Sample #5 were collected at a wavelength of 0.8262 Å by a Mython-II detector on powder diffraction beamline, Australian synchrotron. The powdered samples were loaded into pre-dried 0.7 mm quartz capillaries fitted with a flow cell under an atmosphere of argon. The Rietveld refinement was performed using TOPAS v4.2[32].

The microstructure of $Nd_4Mg_{80}Ni_8$ and its hydrogen-induced microstructure evolution. A bulk sample of $Nd_4Mg_{80}Ni_8$ compound (Sample #6, actual composition is $Nd_{4.5}Mg_{84.6}Ni_{10.9}$) with size of $3 \times 3 \times 2$ mm was polished to obtain a smooth surface. The sample was consist of major phase $Nd_4Mg_{80}Ni_8$ and minor Mg_2Ni. Then the bulk sample was incompletely hydrogenated at 350°C under 2.0 MPa H_2 for 1 h. The microstructure of the sample was examined by FEI Helios Nanolab 600i dual beam focused ion beam FIB. In order to compare the microstructure and phase composition of $Nd_4Mg_{80}Ni_8$ and hydrogenated sample, two thin slices with thickness less than 100 nm were cut from the annealed $Nd_4Mg_{80}Ni_8$ and hydrogenated sample respectively by FEI Helios Nanolab 600i dual beam FIB. SAED patterns and HR-TEM images were collected by Tecnai G2 F20 S-Twin TEM.

The measurement of H/D properties. The H/D properties of annealed $Nd_4Mg_{80}Ni_8$ (Sample #6) was tested using automatic PCT characteristics measurement system from SUZUKI HOKAN. CO., LTD. in Japan. The $Nd_4Mg_{80}Ni_8$ was mechanically crushed into micro-particles (-100 mesh, $<150\mu$m) and activated at 350°C under 4.0 MPa H_2 for hydrogen absorption and at the same temperature in vacuum for hydrogen desorption. The PCT curves were measured at 250 ~ 350°C with the maximum equilibrated time of 40 min. The hydrogen absorption kinetics were examined at 100 ~ 350°C under initial hydrogen pressure of 3.4 MPa. Before hydrogenation the sample was kept in vacuum at 350°C for 2 h to ensure its complete dehydrogenation. The isothermal dehydriding kinetics was examined at 291 ~ 347°C in vacuum after the sample completely hydriding at 350°C for 2 h under initial hydrogen pressure of 3.4 MPa. The cycling behavior of the $Nd_4Mg_{80}Ni_8$ was determined at 300°C. The time for hydriding under initial pressure of 3.0 MPa H_2 was 2 h and for dehydriding in vacuum was 2.8 h. In order to study the relationship between grain size and cycle number, the XRD pattern was collected after the 1st ~ 5th and 10th cycles. The samples were vacuumed at 300°C for 2 h and then air cooled to room temperature. A part of powders after the 5th cycle were further vacuumed at 350°C for 2 h to observe the growth of grain size. The XRD patterns were collected by Bruker AXS D8 diffractometer with Cu Kα radiation. The sizes of the crystallites in the samples were calculated from the refinements of XRD patterns using Scherrer equation.

The evolution of phase composition during hydrogenation. The *in-situ* SR-PXRD data of $Nd_{4.5}Mg_{84.6}Ni_{10.9}$ powders were collected at by a wavelength of 0.8262 Å by a Mython-II detector on powder diffraction beamline, Australian synchrotron. The completely dehydrogenated $Nd_{4.5}Mg_{84.6}Ni_{10.9}$ powders were loaded into pre-dried 0.7 mm quartz capillaries fitted with a flow cell under an atmosphere of argon. The sample was heating to the set temperatures by a Cybostar hot air blower with heating rate of 20°C/min under vacuum, then hydrogen was imported in and the detector started to collect the XRD data. Before heating, the quartz capillaries didn't scrubbing with argon, which led to some oxidation of the sample during heating process. Therefore, about 10.0 wt.% Nd_2O_3 emerged at the initial stage of examination. Then the quantity of Nd_2O_3 didn't change any more. The phase transformation of Mg and Mg_2Ni during the hydriding process still can be observed. The diffraction data under different hydrogen pressures from 0.0 to 2.0 MPa were collected at 350°C and proceeded for 4 min at one pressure. Before every collection, the sample was kept under this pressure for 30 min. The diffraction data at different time was measured every 2 min at 300°C under a constant pressure of 2.0 MPa H_2.

References

1. Schlapbach, L. & Zuttel, A. Hydrogen-storage materials for mobile applications. *Nature* **414,** 353–358 (2001).
2. Weidenthaler, C. & Felderhoff, M. Solid-state hydrogen storage for mobile applications: Quo Vadia? *Energy Environ. Sci.* **4,** 2495–2502 (2011).
3. House, S. D., Vajo, J. J., Ren, C., Rockett, A. A. & Robertson, I. M. Effect of ball-milling duration and dehydrogenation on the morphology, microstructure and catalyst dispersion in Ni-catalyzed MgH_2 hydrogen storage materials. *Acta Mater.* **86,** 55–68 (2015).
4. Cheng, F. Y., Tao, Z. L., Liang, J. & Chen, J. Efficient hydrogen storage with the combination of lightweight Mg/MgH_2 and nanostructures, *Chem. Commun.* **48,** 7334–7343 (2012).
5. Jin, S. A., Shim, J. H., Ahn, J. P., Cho, Y. W. & Yi, K. W. Improvement in hydrogen sorption kinetics of MgH_2 with Nb hydride catalyst, *Acta Mater.* **55,** 5073–5079 (2007).
6. Xie, L., Liu, Y., Wang, Y. T., Zheng, J. & Li, X. G. Superior hydrogen storage kinetics of MgH_2 nanoparticles doped with TiF_3. *Acta Mater.* **55,** 4585–4591 (2007).
7. Denys, R. V., Poletaev, A. A., Solberg, J. K., Tarasov, B. P. & Yartys, V. A. $LaMg_{11}$ with a giant unit cell synthesized by hydrogen metallurgy: Crystal structure and hydrogenation behavior. *Acta Mater.* **58,** 2510–2519 (2010).

8. Lin, H. J. *et al.* Hydrogen storage properties of Mg-Ce-Ni nanocomposite induced from amorphous precursor with the highest Mg content. *Int. J. Hydrogen Energy* **37,** 14329–14335 (2012).

9. Pei, L. C. *et al.* Hydrogen storage properties and phase structures of RMg$_2$Ni (R=La, Ce, Pr, Nd) alloys, *Mater. Sci. Eng. B* **177,** 1589–1595 (2012).

10. Huang, L. J., Liang, G. Y. & Sun, Z. B. Hydrogen-storage propeties of amorphous Mg-Ni-Nd alloys, *J. Alloys Compd.* **421,** 279–282 (2006).

11. Couillaud, S., Gaudin, E. & Bobet, J. L. Rich magnesium ternary compound so-called LaCuMg$_8$ derived from La$_2$Mg$_{17}$. Structure and hydrogenation behavior, *Intermetallics* **19,** 336–341 (2011).

12. Tanaka, K. *et al.* Improvement of hydrogen storage properties of melt-spun Mg-Ni-RE alloys by nanocrystallization, *J. Alloys Compd.* **293-295,** 521–525 (1999).

13. Yin, J. T., Yamada, T., Yoshinari, O. & Tanaka, K., Improvement of hydrogen storage properties of Mg-Ni alloys by rare-earth addition. *Mater. Trans.* **42,** 712–716 (2001).

14. Guénée, L., Favre-Nicolin, V. & Yvon, K. Synthesis, crystal structure and hydrogenation properties of the ternary compounds LaNi$_4$Mg and NdNi$_4$Mg. *J. Alloys Compd.* **348,** 129–137 (2003).

15. Wang, Z. M., Zhou, H. Y., Zou, R. P. & Yao, Q. R. Effect of sintering conditions on the formation of single-phase NdMgNi$_4$ compound and its hydrogen storage properties. *J. Alloys Compd.* **429,** 260–263 (2007).

16. Xie, D. H., Li, P., Zeng, C. X., Sun, J. W. & Qu, X. H. Effect of substitution of Nd for Mg on the hydrogen storage properties of Mg$_2$Ni alloy, *J. Alloys Compd.* **478,** 96–102 (2009).

17. Meng, J. *et al.* A comparative study on effect of microwave sintering and conventional sintering on properties of Nd-Mg-Ni-Fe$_3$O$_4$ hydrogen storage alloy. *Int. J. Hydrogen Energy* **35,** 8310–8316 (2010).

18. Zhang, Q. A., Jiang, C. J. & Liu, D. D. Comparative investigation on the hydrogenation characteristics and hydrogen storage kinetics of melt-spun Mg$_{10}$NiR (R=La, Nd and Sm) alloys. *Int. J. Hydrogen Energy* **37,** 10709–10714 (2012).

19. Huang, J. M. *et al.* Improved hydrolysis properties of Mg$_3$RE hydrides alloyed with Ni. *Int. J. Hydrogen Energy* **39,** 6813–6818 (2014).

20. Denys, R. V. *et al.* In situ synchrotron X-ray diffraction studies of hydrogen desorption and absorption properties of Mg and Mg-Mm-Ni after reactive ball milling in hydrogen. *Acta Mater.* **57,** 3989–4000 (2009).

21. Ouyang, L. Z. *et al.* Enhanced hydrogen storage kinetics and stability by synergistic effects of in Situ Formed CeH$_{2.73}$ and Ni in CeH$_{2.73}$-MgH$_2$-Ni nanocomposites, *J. Phys. Chem. C* **118,** 7808–7820 (2014).

22. Zhang, Q. A. *et al.* Superior hydrogen storage kinetics of Mg$_{12}$YNi alloy with a long-period stacking ordered phase, *Scripta Mater.* **65,** 233–236 (2011).

23. Liu, J. W., Zou, C. C., Wang, H., Ouyang, L. Z. & Zhu, M. Facilitating de/hydrogenation by long-period stacking ordered structure in Mg based alloys. *Int. J. Hydrogen Energy* **38,** 10438–10455 (2013).

24. Denys, R. V. *et al.* Nanostructured rapidly solidified LaMg$_{11}$Ni alloy. II. *In situ* synchrotron X-ray diffraction studies of hydrogen absorption-desorption behaviours. *Int. J. Hydrogen Energy* **37,** 5710–5722 (2012).

25. Poletaev, A. A. *et al.* Nanostructured rapidly solidified LaMg$_{11}$Ni alloy: Microsucture, crystal structure and hydrogenation properties. *Int. J. Hydrogen Energy* **37,** 3548–3557 (2012).

26. Ourane, B. *et al.* The new ternary intermetallic NdNiMg$_5$: Hydrogen sorption properties and more. *Mater. Res. Bull.* **61,** 275–279 (2015).

27. Ourane, B., Gaudin, E., Zouari, R., Couillaud, S. & Bobet, J. L. NdNiMg$_5$, a new magnesium-rich phase with an unusual structural type. *Inorg. Chem.* **52,** 13289–13291 (2013).

28. Hoffmann, R. D., Fugmann, A., Rodewald, U. C. & Pöttgen, R. New Intermetallic Compounds Ln$_2$Ni$_2$Mg (Ln=Y, La-Nd, Sm, Gd-Tm) with Mo$_2$FeB$_2$ Structure. *Z. Anorg. Allg. Chem.* **626,** 1733–1738 (2000).

29. Kadir, K., Noréus, D. & Yamashita, I. Structural determination of AMgNi$_4$ (where A=Ca, La, Ce, Pr, Nd and Y) in the AuBe$_5$ type structure. *J. Alloys Compd.* **345,** 140–143 (2002).

30. Kadir, K., Sakai, T. & Uehara, I. Synthesis and structure determination of a new series of hydrogen storage alloys; RMg$_2$Ni$_9$ (R=La, Ce, Pr, Nd, Sm and Gd) built from MgNi$_2$ laves-type layers alternating with AB$_5$ layers. *J. Alloys Compd.* **257,** 115–121 (1997).

31. Boultif, A. & Louër, D. Powder pattern indexing with the dichotomy method. *J. Appl. Crystallogr.* **37,** 724–731 (2004).

32. TOPAS, BrukerAXS V4. 2, *General profile and structure analysis software for powder diffraction data-user manual.* Karlsruhe, Germany: Bruker AXS (2009).

33. Favre-Nicolin, V. & Černý, R. FOX, 'free objects for crystallography': a modular approach to ab initio structure determination from powder diffraction. *J. Appl. Crystallogr.* **35,** 734–743 (2002).

34. Easton, M. A. *et al.* The role of crystallography and thermodynamics on phase selection in binary magnesium–rare earth (Ce or Nd) alloys. *Acta Mater.* **60,** 4420–4430 (2012).

35. Mulford, R. N. R. & Holley, C. E. J. Pressure-temperature-composition studies of some rare earth/hydrogen system, *J. Phys. Chem.* **59,** 1222–1226 (1955).

36. Toguchi, K., Tada, M. & Huang, Y. C. The effect of the absorption of hydrogen on allotropic transformations in the rare earth metals. *J. Less-Common Met.* **88,** 469–478 (1982).

37. Dornheim, M. *et al.* Hydrogen storage in magnesium-based hydrides and hydride composites. *Scripta Mater.* **56,** 841–846 (2007).

38. Zeng, K., Klassen, T., Oelerich, W. & Bormann, R. Thermodynamic analysis of the hydriding process of Mg-Ni alloys. *J. Alloys Compd.* **283,** 213–224 (1999).

39. Reilly, J. J. & Wiswall, R. H. The reaction of hydrogen with alloys of magnesium and nickel and the formation of Mg$_2$NiH$_4$, *Inorg. Chem.* **7,** 2254–2256 (1968).

40. Nomura, K., Akiba, E. & Ono, S. Kinetics of the reaction between Mg$_2$Ni and hydrogen, *Int. J. Hydrogen Energy* **6,** 295–303 (1981).

41. Gross, K. J., Spatz, P. S., Züttel, A. & Schlapbach, L. Mechanically milled Mg composites for hydrogen storage-The transition to a steady state composition. *J. Alloys Compd.* **240,** 206–213 (1996).

42. Li, Q. *et al.* Characteristics of hydrogen storage alloy Mg$_2$Ni produced by hydriding combustion synthesis. *J. Mater. Sci. Tech.* **20,** 209–212 (2004).

43. Akiba, E., Nomura, K., Ono, S. & Mizuno, Y. Pressure-composition isotherms of MgNiH$_2$ alloys. *J. Less-Common Met.* **83,** L43–L46 (1982).

44. Jander, W. Reaction in the solid state at high temperatures. *Z. Anorg. Allg. Chem.* **163,** 1–30 (1927).

45. Ginstling, A. M. & Brounshtein, B. I. O diffuzionnoi kinetike reaktsii V sfericheskikh chastitsakh. *Zh. Prikl. Khim.* **23,** 1249–1259 (1950).

46. Evard, E., Gabis, I. & Yartys, V. A. Kinetics of hydrogen evolution from MgH$_2$: Experimental studies, mechanism and modelling. *Int. J. Hydrogen Energy* **35,** 9060–9069 (2010).

47. Chou, K. C. & Xu, K. D. A new model for hydriding and dehydriding reactions in intermetallics. *Intermetallics* **15,** 767–777 (2007).

48. Chou, K. C., Luo, Q., Li, Q. & Zhang, J. Y. Influence of the density of oxide on oxidation kinetics. *Intermetallics* **47,** 17–22 (2014).

49. Chou, K. C. & Hou, X. M. Kinetics of high-temperature oxidation of inorganic nonmetallic materials. *J. Am. Ceram. Soc.* **92,** 585–594 (2009).
50. Luo, Q. *et al.* The hydriding kinetics of Mg–Ni based hydrogen storage alloys: A comparative study on Chou model and Jander model. *Int. J. Hydrogen Energy* **35,** 7842–7849 (2010).
51. Li, Q., Chou, K. C., Lin, Q., Jiang, L. J. & Zhan, F. Influence of the initial hydrogen pressure on the hydriding kinetics of the $Mg_{2-x}Al_xNi$ (x=0, 0.1) alloys. *Int. J. Hydrogen Energy* **29,** 1383–1388 (2004).
52. Li, Q. *et al.* Effect of hydrogen pressure on hydriding kinetics in the $Mg_{2-x}Ag_xNi$-H (x=0.05, 0.1) system. *J. Alloys Compd.* **399,** 101–105 (2005).
53. Pan, Y. B., Wu, Y. F. & Li, Q. Modeling and analyzing the hydriding kinetics of Mg-$LaNi_5$ composites by Chou model. *Int. J. Hydrogen Energy* **36,** 12892–12901 (2011).
54. Liu, J., Zhang, X., Li, Q., Chou, K. C. & Xu, K. D. Investigation on kinetics mechanism of hydrogen absorption in the La_2Mg_{17}-based composites. *Int. J. Hydrogen Energy* **34,** 1951–1957 (2009).
55. Liang, G., Huot, J., Boily, S., Van Neste, A. & Schulz, R. Catalytic effect of transition metals on hydrogen sorption in nanocrystalline ball milled MgH_2-Tm (Tm=Ti, V, Mn, Fe and Ni) systems, *J. Alloys Compd.* **292,** 247–252 (1999).

Acknowledgements

Author Contributions

Q.L. conceived of the experiments, analyzed the data, and wrote the manuscript. Q.F.G. contributed to the SR-PXRD measurements and crystal structure analysis. J.Y.Z. contributed to the interpretation of the phase equilibria and TEM results. S.L.C. contributed to the construction of phase diagram. Q.L. and K.C.C. discussed the results. Q.L. designed the experiments, discussed results and wrote the paper. All authors reviewed the manuscript.

Additional Information

Supplementary information accompanies this paper at http://www.nature.com/srep

Competing financial interests: The authors declare no competing financial interests.

How to cite this article: Luo, Q. *et al.* Phase Equilibria, Crystal Structure and Hydriding/Dehydriding Mechanism of $Nd_4Mg_{80}Ni_8$ Compound. *Sci. Rep.* **5**, 15385; doi: 10.1038/srep15385 (2015).